



# Proxima Centauri b: A Strong Case for Including Cosmic-Ray-induced Chemistry in Atmospheric Biosignature Studies

M. Scheucher<sup>1,2</sup> , K. Herbst<sup>3</sup> , V. Schmidt<sup>4</sup>, J. L. Grenfell<sup>2</sup> , F. Schreier<sup>5</sup> , S. Banjac<sup>3</sup>, B. Heber<sup>3</sup> , H. Rauer<sup>1,2,6</sup>, and M. Sinnhuber<sup>4</sup> 

<sup>1</sup> Zentrum für Astronomie und Astrophysik, Technische Universität Berlin, D-10623 Berlin, Germany; [scheucher@tu-berlin.de](mailto:scheucher@tu-berlin.de), [markus.scheucher@dlr.de](mailto:markus.scheucher@dlr.de)

<sup>2</sup> Institut für Planetenforschung, Deutsches Zentrum für Luft- und Raumfahrt, D-12489 Berlin, Germany

<sup>3</sup> Institut für Experimentelle und Angewandte Physik, Christian-Albrechts-Universität zu Kiel, D-24118 Kiel, Germany

<sup>4</sup> Institut für Meteorologie und Klimaforschung, Karlsruher Institut für Technologie, D-76344 Eggenstein-Leopoldshafen, Germany

<sup>5</sup> Institut für Methodik der Fernerkundung, Deutsches Zentrum für Luft- und Raumfahrt, D-82234 Oberpfaffenhofen, Germany

<sup>6</sup> Institut für Geologische Wissenschaften, Freie Universität Berlin, D-12249 Berlin, Germany

Received 2019 December 10; revised 2020 February 19; accepted 2020 February 28; published 2020 April 8

## Abstract

Due to its Earth-like minimum mass of  $1.27 M_E$  and its close proximity to our solar system, Proxima Centauri b is one of the most interesting exoplanets for habitability studies. Its host star, Proxima Centauri, is however a strongly flaring star, which is expected to provide a very hostile environment for potentially habitable planets. We perform a habitability study of Proxima Centauri b assuming an Earth-like atmosphere under high stellar particle bombardment, with a focus on spectral transmission features. We employ our extensive model suite calculating energy spectra of stellar particles, their journey through the planetary magnetosphere, ionosphere, and atmosphere, ultimately providing planetary climate and spectral characteristics, as outlined in Herbst et al. Our results suggest that together with the incident stellar energy flux, high particle influxes can lead to efficient heating of the planet well into temperate climates, by limiting  $\text{CH}_4$  amounts, which would otherwise run into antigreenhouse for such planets around M stars. We identify some key spectral features relevant for future spectral observations: First,  $\text{NO}_2$  becomes the major absorber in the visible, which greatly impacts the Rayleigh slope. Second,  $\text{H}_2\text{O}$  features can be masked by  $\text{CH}_4$  (near-infrared) and  $\text{CO}_2$  (mid- to far-infrared), making them nondetectable in transmission. Third,  $\text{O}_3$  is destroyed and instead  $\text{HNO}_3$  features become clearly visible in the mid- to far-infrared. Lastly, assuming a few percent of  $\text{CO}_2$  in the atmosphere,  $\text{CO}_2$  absorption at  $5.3 \mu\text{m}$  becomes significant (for flare and nonflare cases), strongly overlapping with a flare related  $\text{NO}$  feature in Earth's atmosphere.

*Unified Astronomy Thesaurus concepts:* [Exoplanets \(498\)](#); [Atmospheric science \(116\)](#); [Cosmic rays \(329\)](#); [Exoplanet atmospheric composition \(2021\)](#); [Exoplanet atmospheres \(487\)](#); [Photoionization \(2060\)](#); [Biosignatures \(2018\)](#)

## 1. Introduction

Given the recent, exciting discoveries of terrestrial-sized planets orbiting M stars, together with the higher activity of many M stars compared to our Sun (e.g., Reid & Hawley 2005; Scalo et al. 2007), a better understanding of the influence and impact of such active host stars upon planetary habitability is crucial for the search for extraterrestrial life and improving our understanding of Earth-like planets. Proxima Centauri b (hereafter Prox Cen b) is one of the most interesting exoplanets to date in terms of studying potential habitability (see, e.g., Turbet et al. 2016; Dong et al. 2017; Meadows et al. 2018; Berdyugina & Kuhn 2019). With a minimum of 1.27 Earth masses (Anglada-Escudé et al. 2016), it may be similar in bulk properties to Earth. Although it receives only 65% of the mean total stellar irradiation (TSI) compared to Earth, Meadows et al. (2018) showed that an Earth-like atmosphere with, e.g., a surface carbon dioxide concentration of a few percent could lead to habitable conditions.

Proxima Centauri (hereafter Prox Cen), is an M5.5Ve flaring star. While direct observations of coronal mass ejections (CMEs) and corotating interaction regions (CIRs) are still challenging, model extrapolations from the Sun's flare–CME correlation can be used to estimate the bombardment by stellar energetic particles (SEP). While the planetary magnetosphere could shield the planet from the majority of low-energy SEPs, the multitude of flares—and possible CMEs—of active M stars

may cause long-lasting changes to the planet's atmospheric mass, composition, and surface conditions (e.g., Vidotto et al. 2013). There is an ongoing debate as to whether such close-in planets orbiting active M stars would be stripped of their atmospheres, e.g., if they lie within the star's Alfvén sphere, leaving them without magnetospheric protection (e.g., Lammer et al. 2010; Airapetian et al. 2017a).

Including the impact of stellar high energetic particles in habitability studies in a self-consistent way requires a broad understanding of stellar, astrospheric, magnetospheric, and ion and neutral chemical processes within the planet's atmosphere. Modeling efforts by, e.g., Segura et al. (2010), Grenfell et al. (2012), Tabataba-Vakili et al. (2016), Tilley et al. (2019), and Scheucher et al. (2018) have parameterized the top-of-atmosphere (TOA) incoming particle energy distributions, secondary particle generation in air showers, ionization of the atmosphere, and its impact on neutral atmospheric composition, using different methods. Herbst et al. (2019a) took this one step further by coupling cosmic-ray-induced magnetospheric, ionospheric, and lower atmospheric processes in an interactive model suite.

Such studies are crucial in order to understand the expected range of atmospheres of such planets lying in—or close to—the habitable zone, as well as to better understand and interpret atmospheric spectra of next generation space missions such as the *James Webb Space Telescope (JWST)*, *HabEX*, and

*LUVVOIR*, plus ground-based telescopes like the Extremely Large Telescope (ELT).

## 2. Methodology

We apply the comprehensive model suite described in Herbst et al. (2019a) to study the habitability of Prox Cen b as influenced by the strong stellar activity of its host star.

### 2.1. Initial Atmosphere

We use our 1D climate-chemistry model (1D CCM; see, e.g., Rauer et al. 2011; von Paris et al. 2015; Scheucher et al. 2018) to calculate initial climate and neutral atmospheric composition for Prox Cen b without SEP or galactic cosmic-ray (GCR) impacts. The stellar energy spectrum is taken from the Virtual Planetary Laboratory Spectral Database,<sup>7</sup> described in Meadows et al. (2018), and the incoming stellar irradiation is scaled to Prox Cen b’s distance of 0.0485 au. To build our planet, we start with the observed minimum mass of  $1.27 M_E$  and use the mass–radius relationship from Valencia et al. (2007) with an Earth-like ice-mass fraction of 0.1%, which results in a radius  $R$  of  $1.065 R_E$  and a surface gravity  $g_{\text{surf}}$  of  $10.98 \text{ m s}^{-2}$  via  $m R^{-2}$ .

We start with the Earth US standard 1976 atmosphere (Committee on Extension to the Standard Atmosphere—COESA) and increase the surface pressure to  $p_{\text{surf}} = 1.119 \text{ bar}$ , in order to maintain Earth’s atmospheric mass. We use Earth reference surface fluxes in our model similar to Segura et al. (2005) and Meadows et al. (2018) which result in the modern-Earth 1976 surface mixing ratios of 1.5 ppm  $\text{CH}_4$ , 190 ppm  $\text{CO}$ , and 270 ppm  $\text{N}_2\text{O}$ . This is achieved in our chemical scheme with  $8.2 \times 10^{10} \text{ CH}_4$ ,  $1.8 \times 10^{11} \text{ CO}$ , and  $1.1 \times 10^9 \text{ molecules cm}^{-2} \text{ s}^{-1} \text{ N}_2\text{O}$ . These fluxes together with initial surface mixing ratios of 500 ppm  $\text{H}_2$ , 21.1%  $\text{O}_2$ , and 0.934% Ar are used as boundary conditions for all our Prox Cen b runs. With cloud-free conditions and a basaltic surface albedo of  $A_{\text{surf}} = 0.13$ , we increase the  $\text{CO}_2$  amount in the atmosphere by replacing  $\text{N}_2$  with  $\text{CO}_2$  step-by-step. Our aim is to investigate potential surface habitability. We start with 5%  $\text{CO}_2$  (72.4%  $\text{N}_2$ ) and increase in steps of 5% up to 20%  $\text{CO}_2$  (57.4%  $\text{N}_2$  respectively). The tropospheric temperatures and water amounts are calculated via adiabatic lapse rates after Manabe & Wetherald (1967) with a surface relative humidity,  $\text{RH} = 80\%$ . For kinetic transport in the chemistry calculations we use eddy diffusion parameterized for Earth after Massie & Hunten (1981).

### 2.2. Galactic and Stellar Cosmic-Ray Spectra

To model the impact of energetic particles on planetary atmospheres both GCRs and SEPs have to be considered. Since Prox Cen is our nearest neighbor it is reasonable to assume the same local interstellar medium (LISM) conditions as for our Sun. However, analytical studies by Struminsky et al. (2017) and Sadovskii et al. (2018) showed that GCRs with energies below 1 TeV are not able to reach Prox Cen b. Besides, the flux of such high energetic GCR particles in the LISM is vanishingly small and can be neglected to a first-order approximation. However, due to the high stellar activity of Prox Cen, SEPs most likely have a strong impact on Prox Cen

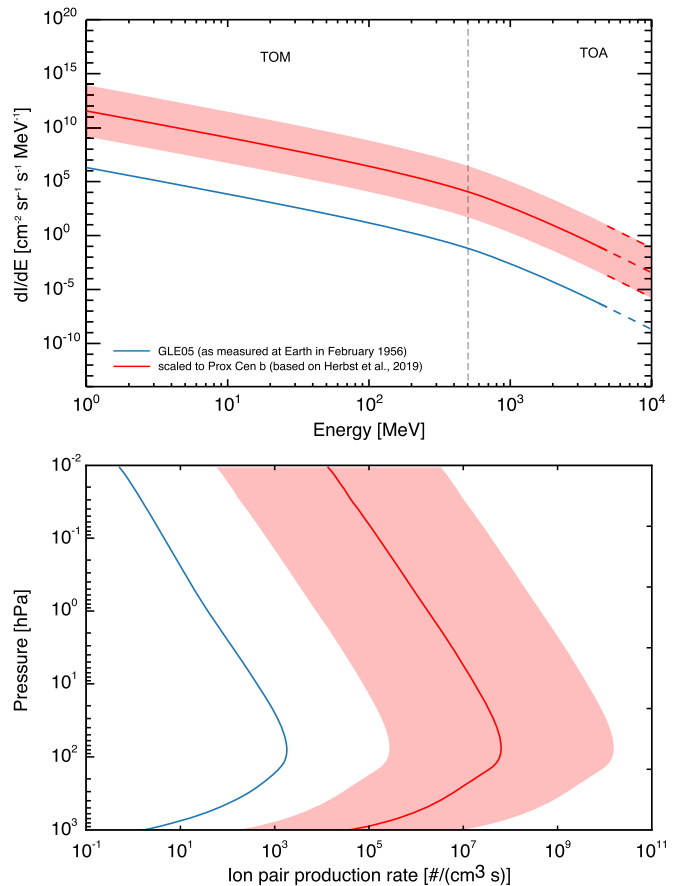


**Figure 1.** Upper panel: observed GLE event spectrum of GLE05 (blue) compared to the scaled event spectrum at Prox Cen b (red) including the corresponding error band (red shaded region) and cutoff energy on TOA (gray dashed). Lower panel: corresponding event-induced atmospheric ion-pair production rates at Earth (blue) and at Prox Cen b (red).

b. For example, Howard et al. (2018) most recently found strong optical flares with intensities at 0.0485 au of up to  $92 \text{ W m}^{-2}$  on Prox Cen. Herbst et al. (2019b) suggested that such high flare intensities correspond to stellar proton fluences of  $10^8$ – $10^{14}$  protons/( $\text{cm}^2 \text{ sr s}$ ) around Prox Cen at 0.048 au. To derive our actual particle spectrum, we scale from a well-known measured event spectrum. Our study is based on one of the strongest events measured on Earth, the ground level enhancement (GLE) of 1956 February (GLE05, see the upper panel of Figure 1).

### 2.3. Planetary Magnetic Field and Atmospheric Ionization

From Earth we know that low-energetic particles are deflected by the geomagnetic field which acts as an additional particle filter. Thus, the CR flux at the top of the magnetosphere (TOM) is not the same as that at the TOA, which further depends on the magnitude and geometry of the planetary magnetic field (see, e.g., Herbst et al. 2013).

Assuming an Earth-like magnetic field, the so-called cutoff rigidity  $R_c$ , an equivalent to the energy that particles require to enter the atmosphere at a given location, is computed with PLANETOCOSMICS (see, e.g., Desorgher et al. 2006). As a first-order approximation, in this study we utilize the implemented International Geomagnetic Reference Field (see, e.g., Thébault et al. 2015) model to describing the modern-Earth internal terrestrial magnetic field. The globally distributed

<sup>7</sup> <http://depts.washington.edu/naivpl/content/spectral-databases-and-tools>

cutoff rigidity values have been modeled based on the highest planetary disturbance value ( $k_p > 7$ ). However, since no information on the spatial resolution of the exoplanetary atmospheric transmission is available, in this study, we assume planetary midlatitudes around  $60^\circ$ , corresponding to a mean cutoff rigidity of 1.11 GV (around 510 MeV), as indicated by the dashed line in the upper panel of Figure 1. As can be seen, this cutoff separates the TOM from the TOA spectrum.

However, we note that the magnetospheric structure of Prox Cen b could be different from that of the Earth, for example, due to strong Joule heating caused by fast stellar winds impinging on the upper planetary atmosphere (see, e.g., Cohen et al. 2014).

Nevertheless, energetic charged particles that reach the planetary atmosphere will lose energy due to collisions with the surrounding atmospheric constituents, resulting in an ionization of the upper planetary atmosphere. Further, interactions with, for example, nitrogen, oxygen, or argon atoms might trigger the development of a secondary particle shower and associated photochemical effects. The deeper a particle is able to enter into the atmosphere, the more likely a collision with these species becomes. The generated secondary particles may further interact, resulting in the formation of atmospheric particle cascades (see, e.g., Dorman et al. 2004) and an altitude-dependent atmospheric ionization. This, however, strongly depends on the type and energy of the primary particle, the atmospheric altitude, and the location.

Neglecting GCRs and their astrospheric modulation, the SEP-induced ionization rates  $Q$  can numerically be described by

$$Q(E_c, x) = \sum_i \int_{E_c}^{E_u} J_i(E) \cdot Y_i(E, x) dE, \quad (1)$$

with  $i$  representing the primary particle type,  $E_u$  the upper energy of the stellar particle event,  $J_i$  the stellar differential particle event spectrum, and  $Y_i$  the so-called atmospheric ionization yield function given as  $\alpha \cdot \frac{1}{W_{\text{ion}}} \frac{\Delta E_i}{\Delta x}$ , where  $\frac{\Delta E_i}{\Delta x}$  reflects the mean specific energy loss, while  $W_{\text{ion}}$  represents the atmospheric ionization energy (see, e.g., Porter et al. 1976; Simon Wedlund et al. 2011).

The event-dependent atmospheric ionization rates are modeled with the newly developed Atmospheric Radiation Simulator (AtRIS, see Banjac et al. 2019), utilizing the provided planetary and atmospheric conditions, as well as the particle event spectrum.

#### 2.4. Impact on Atmospheric Ionization, Neutral Chemistry, and Climate

The impact of ionization on neutral composition is modeled with the 1D Exoplanetary Terrestrial Ion Chemistry model (ExoTIC; Herbst et al. 2019a, based on the UBI model described, e.g., in Winkler et al. 2009; Sinnhuber et al. 2012; Nieder et al. 2014), taking global averages of the particle-induced ionization calculated by AtRIS (Banjac et al. 2019). ExoTIC considers 60 neutral and 120 ion species for neutral, neutral-ion, and photochemical reactions. Primary ions as well as excited species are provided from the ionization, dissociation and dissociative ionization of  $\text{O}_2$ ,  $\text{N}_2$ , and  $\text{O}$ ; an increase in  $\text{CO}_2$  mixing ratios may therefore lower the amount of primary ions from  $\text{N}_2$ ,  $\text{O}_2$ , and  $\text{O}$ , but  $\text{CO}_2$  dissociative ionization is not considered.

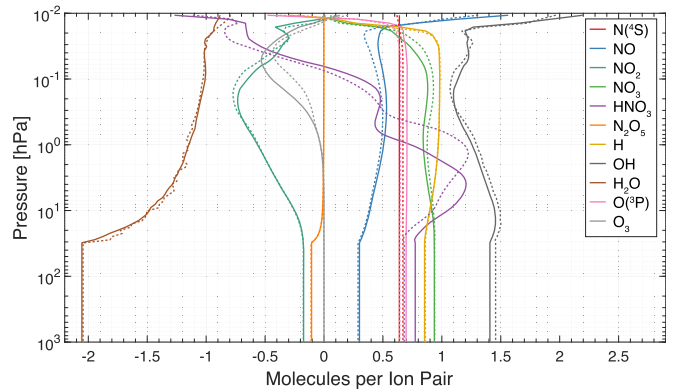


**Figure 2.** Production and loss rates of neutral species due to ion-chemistry processes calculated with ExoTIC for the 5%  $\text{CO}_2$  (solid) and 20%  $\text{CO}_2$  (dotted) atmospheres for the GLE05 event scaled to Prox Cen b. Below 30 hPa, rates are set to isoprofiles.

Both particle-induced ionization and the production and loss rates of NOx ( $\text{N}(^2\text{D})$ ,  $\text{N}(^4\text{S})$ ,  $\text{NO}$ ,  $\text{NO}_2$ ,  $\text{NO}_3$ ,  $\text{N}_2\text{O}_5$ ), HOx ( $\text{H}$ ,  $\text{OH}$ ),  $\text{HNO}_3$ ,  $\text{H}_2\text{O}$ ,  $\text{O}_3$ ,  $\text{O}(^3\text{P})$ , and  $\text{O}(^1\text{D})$  per initial ion, are then transferred from ExoTIC to the 1D CCM, which produces atmospheric climate and composition under SEP and GCR bombardment as input for the next iteration with AtRIS and ExoTIC. Planetary conditions are considered to be in equilibrium when neither ionization, redistribution rates, nor atmospheric conditions change.

#### 2.5. Spectral Characteristics

For spectral analysis we supply output ( $p$ ,  $T$ , composition) from the coupled model suite as input into the “Generic Atmospheric Radiation Line-by-line Infra-red Code” (GARLIC; e.g., Schreier et al. 2014, 2018a, 2018b) using HITRAN2016 (Gordon et al. 2017), CKD continua derived from Clough et al. (1989), visible and near-infrared (IR) cross sections from the Mainz Spectral Atlas (Keller-Rudek et al. 2013), and Rayleigh scattering parameterization from Snee & Ubachs (2005), Marcq et al. (2011), and Murphy (1977).

### 3. Results

The upper panel of Figure 1 shows the energy spectrum of GLE05 at Earth (blue) and its scaling to the energy spectrum at Prox Cen b (red, see Herbst et al. 2019b); the lower panel displays the corresponding cosmic-ray-induced ion-pair production rate calculated for the GLE05 from Earth scaled to Prox Cen b for the initial atmospheres described in Section 2.1. We see the typical ion-pair production peak in the lower stratosphere due to increasing atmospheric density.

Figure 2 shows the ion-chemistry response for the species submitted from the ion-chemistry model to the 1D CCM. Tropospheric values are set to constants based on the lowermost stratospheric values. Rates for  $\text{H}$  and  $\text{N}(^4\text{S})$  are similar to Earth-like values of 1 and 0.6 respectively (compare, e.g., Sinnhuber et al. 2012; Herbst et al. 2019a), while values, e.g., for  $\text{NO}$  and  $\text{OH}$  are different. The  $\text{NO}$  formation rate is smaller than on Earth ( $< 0.58$  compared to  $\sim 0.58$ ), with values for the 20%  $\text{CO}_2$  atmosphere being smaller than for the 5%  $\text{CO}_2$  case, indicating that this difference is due to the change in bulk atmosphere. The  $\text{OH}$  formation rate is distinctly larger than for Earth ( $\sim 1.5$  compared to  $\leq 1$ ), with values for the 20%  $\text{CO}_2$  case larger than for the 5%  $\text{CO}_2$  case, again indicating that

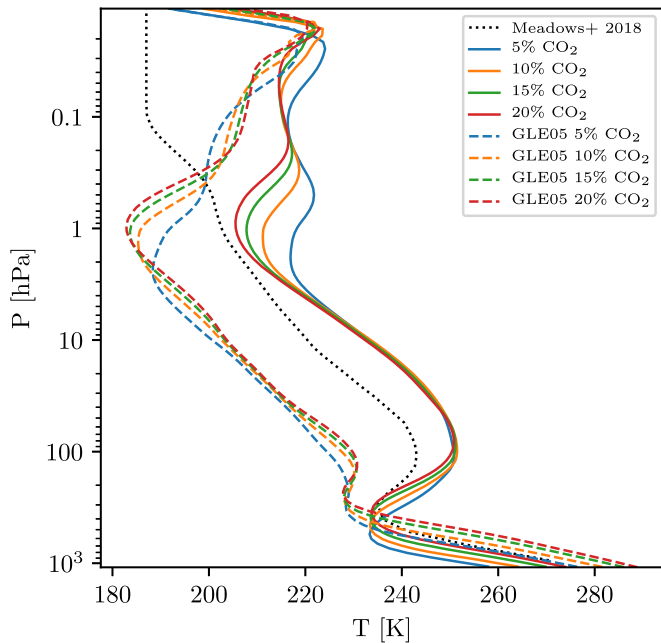


**Figure 3.** Atmospheric temperature profiles for an Earth-like Prox Cen b with varying amounts (vmr) of atmospheric CO<sub>2</sub> (colors). We compare results for a virtually quiescent Prox Cen (solid) with a high flaring host star (dashed). Overplotted (black dotted) are results from Meadows et al. (2018).

this difference is due to the change in bulk atmospheric composition. Further analysis shows that the formation rates of NO and OH from positive ion-chemistry reactions are similar to Earth values, while those from negative ion chemistry are very different (not shown). Note the strong changes of the formation rates of HNO<sub>3</sub> and O<sub>3</sub> between the 5% and 20% CO<sub>2</sub> cases. This might indicate that the different formation rates of OH and NO on Earth may be due to a different composition of negative NO<sub>3</sub><sup>-</sup> containing cluster ions which also play a role in HNO<sub>3</sub> formation via recombination (e.g., Sinnhuber et al. 2012). This demonstrates the importance of considering the full ion chemistry even for Earth-like (O<sub>2</sub>-N<sub>2</sub>) atmospheres.

Figure 3 shows temperature profiles for scenarios having Earth-like atmospheres but with varying amounts of CO<sub>2</sub> for quiescent stellar conditions (solid lines) and with GCRs and SEPs based on GLE05 (dashed lines). Figure 3 suggests CO<sub>2</sub> greenhouse warming in the lower atmosphere together with associated mesospheric cooling. Associated with the weak stellar irradiation, results suggest 20% mixing ratio by volume (vmr) of CO<sub>2</sub> is needed in the nonflare cases to achieve global average temperatures that support liquid surface water. In the middle atmosphere, results suggest that the temperature is not sensitive to changes in CO<sub>2</sub>. A comparison of our 5% CO<sub>2</sub> run (solid blue) with Meadows et al. (2018) who assumed an Earth-like Prox Cen b with 5% CO<sub>2</sub> and who did not consider cosmic rays (black dotted), generally shows reasonable agreement, although some differences arise due to the different assumptions used for CH<sub>4</sub> surface fluxes. Our model with post-industrial surface fluxes (solid blue line, 5% CO<sub>2</sub> in Figure 4) yields CH<sub>4</sub> concentrations of ~5300 ppm, while Meadows et al. (2018) reported ~1000 ppm with lower preindustrial CH<sub>4</sub> fluxes. In our model this leads to a stronger CH<sub>4</sub> antgreenhouse, hence lower surface temperatures with a warmer stratosphere.

Figure 3 additionally shows (dashed lines) atmospheric temperatures for flaring scenarios of Prox Cen with the

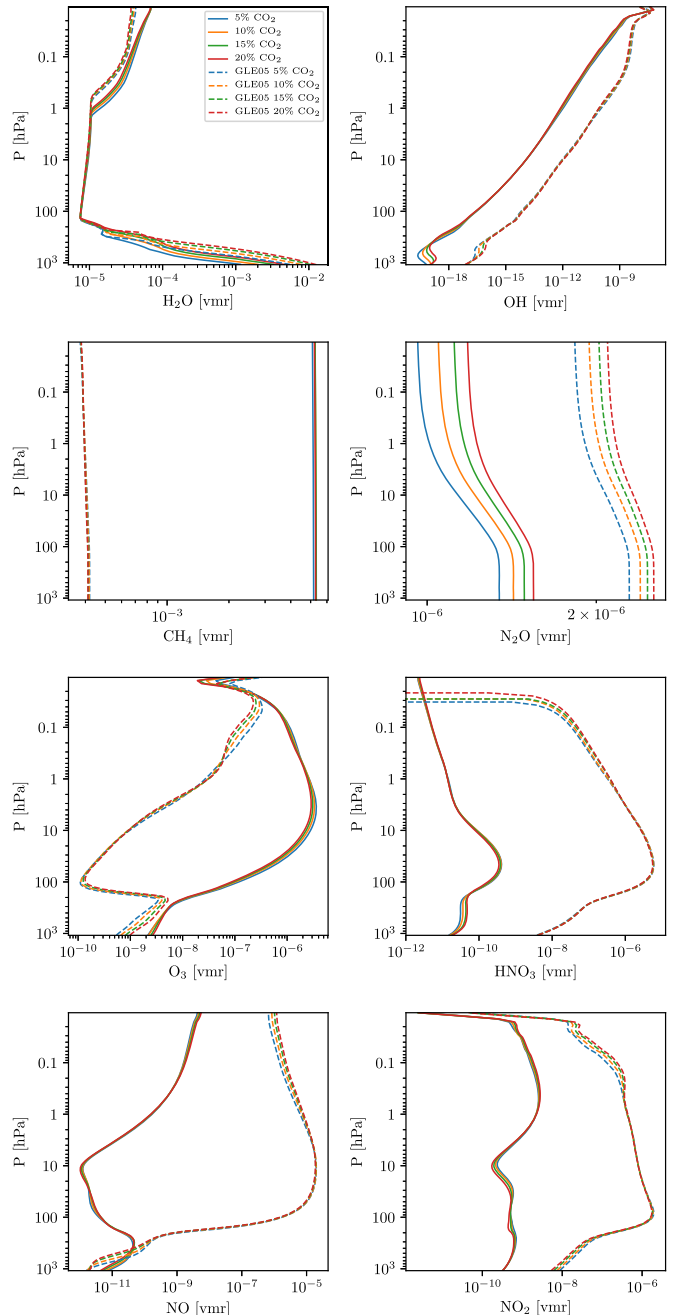


**Figure 4.** Volume mixing ratios of H<sub>2</sub>O, OH, CH<sub>4</sub>, N<sub>2</sub>O, O<sub>3</sub>, HNO<sub>3</sub>, NO, and NO<sub>2</sub> for the scenarios of Figure 3.

calculated GLE05 induced ionization from Figure 1 and chemical production/loss rates from Figure 2. Surface CH<sub>4</sub> here is decreased from 5300 down to 400 ppm (although CH<sub>4</sub> vmr are still essentially isoprofiles as shown in Figure 4), yielding a weaker antgreenhouse effect, resulting in higher surface temperatures for the flaring cases. Interestingly, all four tested CO<sub>2</sub> concentrations are sufficient for the flaring cases to warm the surface and lead to habitable conditions. The 15% CO<sub>2</sub> scenario outputs Earth-like 288 K global average surface temperatures.

Figure 4 shows atmospheric vmr profiles of H<sub>2</sub>O, OH, N<sub>2</sub>O, O<sub>3</sub>, HNO<sub>3</sub>, NO, and NO<sub>2</sub> for the quiescent and flaring cases from Figure 3. Our CH<sub>4</sub> abundances are strongly

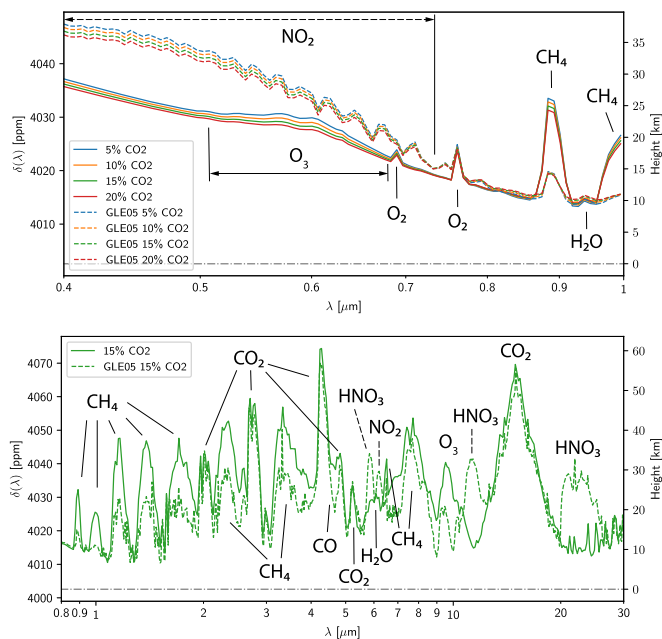


**Figure 5.** Upper: transmission spectra ( $R = 100$ ) from 400 to 1000 nm for the scenarios shown in Figures 3 and 4. Lower: IR transmission spectral comparison for the two 15% CO<sub>2</sub> scenarios, the quiescent host star (solid), and GLE05 conditions (dashed).

increased compared to Earth. This arises (see Segura et al. 2005) due to lower UVB radiation which lowers O<sub>3</sub> photolysis; this then lowers O(<sup>1</sup>D) (a product of O<sub>3</sub> photolysis), which lowers the rate of H<sub>2</sub>O + O(<sup>1</sup>D), and hence lowers OH and increases CH<sub>4</sub>. For the flaring cases, however, CH<sub>4</sub> is effectively reduced by high amounts of cosmic-ray-induced OH, via CH<sub>4</sub> + OH → CH<sub>3</sub> + H<sub>2</sub>O. Stratospheric ozone strongly decreases similarly to Scheucher et al. (2018). Increases in OH and NO (which can remove stratospheric ozone and stimulate smog ozone) for the flaring cases are a result of the cosmic-ray-induced production rates from ion redistribution into neutral species. HNO<sub>3</sub> increases by up to four orders of magnitude compared to the nonflaring case, mostly due to photochemistry (its main in situ source is via the reaction: NO<sub>2</sub> + OH + M → HNO<sub>3</sub> + M (“M” refers to any third body)). The gas-phase precursors of HNO<sub>3</sub>, i.e., NO<sub>2</sub> and OH, are stimulated by cosmic-ray-induced chemistry. H<sub>2</sub>O does not show significant changes in molecular abundance. NO<sub>2</sub> shows up to four orders of magnitude increased concentrations for the flaring compared to the quiescent case. Figure 2 shows cosmic-ray-induced ion-chemical destruction of NO<sub>2</sub>. NO<sub>2</sub> is incorporated into cluster ions which release other N-containing species under recombination, either NO, NO<sub>3</sub>, or HNO<sub>3</sub>, which then form NO<sub>2</sub> in a multitude of secondary neutral gas-phase reactions, overwhelming the apparent loss. One important source is the higher UVB radiation environment in the lower-middle atmosphere because of the lowered O<sub>3</sub> concentration, hence reduced UVB absorption. This increases photolysis of, most importantly, HNO<sub>3</sub>, HO<sub>2</sub>NO<sub>2</sub>, and N<sub>2</sub>O<sub>5</sub>, producing large amounts of NO<sub>2</sub>. Further, NO<sub>2</sub> is a direct product of the O<sub>3</sub> destruction mechanism starting with NO + O<sub>3</sub> → NO<sub>2</sub> + O<sub>2</sub>, and cosmic-ray-induced NO<sub>x</sub> and HO<sub>x</sub> also contribute significantly via the two reactions NO + HO<sub>2</sub> → NO<sub>2</sub> + OH and NO + NO<sub>3</sub> → 2NO<sub>2</sub>. N<sub>2</sub>O, on the contrary, does not show changes due to cosmic rays significant enough to show up in

our simulated spectra (Figure 5). The ~65% increase in overall abundance in Figure 4 for our flaring cases compared to the quiescent runs is a little counterintuitive at first, because with the large decrease in O<sub>3</sub> amounts the overall UVB and UVC radiation environment, i.e., photolysis of other species, increases. Our analysis showed that UVC fluxes <198 nm are decreased significantly, reducing N<sub>2</sub>O photolysis—the major N<sub>2</sub>O sink in our model. From a detailed investigation of changes in molecular abundances of other major absorbers overlapping in wavelength range with N<sub>2</sub>O photolysis (significant ~175–240 nm), together with their photolysis cross sections, showed a steep increase of HNO<sub>3</sub> and NO<sub>2</sub> (and some increase for HO<sub>2</sub>NO<sub>2</sub> below ~20 hPa) photolysis rates, hence shielding of N<sub>2</sub>O. Small changes in N<sub>2</sub>O with the variation of CO<sub>2</sub> contents are most importantly related to temperature changes, i.e., H<sub>2</sub>O steam amounts and photolysis rates in the atmosphere.

Figure 5 shows synthetic transmission spectra calculated by GARLIC. The visible to near-IR (Figure 5, upper panel) is a key region, e.g., for biosignature studies of, for example, O<sub>2</sub> with the ELT (e.g., Rodler & López-Morales 2014; Snellen 2014). Bétrémieux & Kaltenegger (2013) noted the importance of including, for example, O<sub>2</sub> and O<sub>3</sub> absorption in this region, which is overlooked by many biosignature studies, but which is included in our work. Our results (Figure 5, upper panel) suggest a significant difference between the flaring and quiescent runs—but smaller differences due to changing composition for the individual flaring or quiescent runs. All quiescent runs show the O<sub>3</sub> Chappuis bands around 600 nm known from Earth, with minor differences in strength, due to the slightly different strato-/mesospheric O<sub>3</sub> amounts. This absorption feature is rather small compared with Earth’s atmosphere because of the generally lower O<sub>3</sub> amounts of ~70 Dobson units for the quiescent case. In the flaring runs, there is a striking broad absorption feature from ~400 to 700 nm attributed to NO<sub>2</sub>. Due to high amounts of cosmic-ray-induced NO<sub>2</sub>, these features act almost as a continuum in the visible (making the sky brownish-red), stronger than the 600 nm O<sub>3</sub> feature previously mentioned, and could potentially be misinterpreted as a steeper Rayleigh slope. We propose the NO<sub>2</sub> feature as a spectral “marker” of N<sub>2</sub>-O<sub>2</sub> atmospheres which are subject to cosmic rays (see also Airapetian et al. 2017b).

The IR spectrum (Figure 5, lower panel) shows a direct comparison of the 15% CO<sub>2</sub> runs, where the flaring case leads to Earth-like temperatures of 288 K in Figure 3. Again, the effect of varying composition was minor (not shown). As expected, the CH<sub>4</sub> features in the mid IR, coinciding with H<sub>2</sub>O features, are significantly reduced because of reduced CH<sub>4</sub> in the flaring runs. Similar to Tabataba-Vakili et al. (2016) and Scheucher et al. (2018), strong flare features from HNO<sub>3</sub> occur around 11 and 21 μm, but the O<sub>3</sub> absorption feature around 9.6 μm is greatly reduced.

Around 5.3 μm, we see a narrow but distinct absorption feature around 10 ppm (in  $\delta(\lambda)$ ) above the lower-atmosphere H<sub>2</sub>O absorption background. On the modern Earth, there is a band at 5.3 μm from NO via stratospheric N<sub>2</sub>O oxidation which varies considerably with geomagnetic activity, due to fast solar wind, CIRs and CMEs, as well as from extra NO production in the upper mesosphere/lower thermosphere from far-UV and EUV photoionization, and particle impact ionization. Therefore the strength of this NO feature can be treated

as an SEP indicator in Earth’s atmosphere (see, e.g., Airapetian et al. 2017b). However, in our modeled spectra, this feature (peaking at  $5.35 \mu\text{m}$ ) has the same strength for both the flaring and the quiescent cases. We identified this as a weak absorption band of  $\text{CO}_2$ , which generally receives little attention in the literature, e.g., because of the much stronger  $\text{CO}_2$  bands in the spectral vicinity at  $4.3$  and  $4.8 \mu\text{m}$ . This  $5.3 \mu\text{m}$  spectral feature could therefore lead to misinterpretation of future observations because of the above discussed clear correlation with flares in Earth’s atmosphere.

It is striking that there is no single significant  $\text{H}_2\text{O}$  feature in the spectrum. We tested this up to *JWST*-like spectral resolutions of  $R = 3000$  in the near-IR (not shown) by removing  $\text{H}_2\text{O}$  absorption from the spectrum. The resulting spectra showed differences of no more than 2 ppm (in  $\delta(\lambda)$ ) in selected  $\text{CH}_4$  window regions.  $\text{H}_2\text{O}$  concentrations in an Earth-like troposphere decrease rapidly with height with the existence of a cold trap, hence major  $\text{H}_2\text{O}$  absorption features arise lower down in the atmosphere. For example, in the  $15 \mu\text{m}$   $\text{CO}_2$  band  $\text{H}_2\text{O}$  would become optically thick at 28 km in our runs shown in Figure 5, whereas  $\text{CO}_2$  makes the atmosphere opaque at heights of 61 km in transmission; thus, the absorption due to  $\text{H}_2\text{O}$  could not be measured. Similarly, between 1 and  $4 \mu\text{m}$  all  $\text{H}_2\text{O}$  absorption bands are overlapped by strong  $\text{CH}_4$  absorption, which makes the atmosphere opaque at around 40 km. It is noteworthy, that in the absence of SEPs there is a weak feature from the  $\text{H}_2\text{O}$  absorption band around  $6 \mu\text{m}$  as pointed out by Meadows et al. (2018) and indicated in Figure 5, which would be difficult to distinguish from background noise in our simulations.

#### 4. Summary

We performed a habitability study of Prox Cen b assuming an Earth-like atmosphere, focusing on the influence of SEPs from stellar flares upon spectral transmission features. We applied our extensive model suite discussed in Herbst et al. (2019a), which includes the calculation of SEP fluxes and spectral energy distributions, their precipitation through a planetary magnetosphere and atmosphere, cosmic-ray-induced atmospheric ionization, ion redistribution within the atmosphere, and atmospheric climate and neutral composition. Our results suggest a few words of caution for the analysis of spectra from future observations of such planets around M-dwarf stars.

Given the general lack of in situ particle measurements from flaring events of Prox Cen, we scale the known SEP flux of GLE05 measured at Earth to the intensity of the measured flare (Herbst et al. 2019b) and the orbit of Prox Cen b, then calculate the ion-pair production in a theoretical Earth-like atmosphere with elevated  $\text{CO}_2$  amounts in order to warm the planet at its position of 0.65 TSI. Together with the production and loss rates of neutral species from the redistribution of cosmic-ray-induced ions, we find steady-state climate and atmospheric compositions that enable liquid surface water. Our results suggest that SEPs might play a crucial role in efficiently warming such planets, which would otherwise be too cold to be habitable (by reducing the antigreenhouse gas  $\text{CH}_4$ ). Numerous studies (e.g., Segura et al. 2005; Rauer et al. 2011) have suggested that planets with Earth-like biomasses could develop methane abundances orders of magnitude higher than on Earth because of the different stellar spectrum (especially the reduced

UVB), which can then lead to antigreenhouse methane cooling (see Figure 3).

By including SEPs from stellar flares, strong production of cosmic-ray-induced OH efficiently reduces  $\text{CH}_4$ , hence results in temperate global average surface temperatures for all our test atmospheres. This result is exciting because strong SEPs and flares are generally considered to be unfavorable for planetary habitability, because of potentially increased atmospheric escape and increases in surface dosage. We suggest that the habitability of Earth-like planets near the outer habitable zone (HZ) of cooler stars could depend strongly on both,  $\text{CH}_4$  and  $\text{CO}_2$ . Methane, in turn, can be sensitive to cosmic-ray-induced chemistry.

We identify some key features in our synthetic planetary transmission spectra (Figure 5), some related to SEPs, and note some cautions related to the possible misinterpretation of future spectral observations.

1.  $\text{N}_2\text{-O}_2$ -dominated atmospheres could produce large cosmic-ray-induced amounts of  $\text{NO}_2$ , strongly absorbing between 400 and 700 nm. This could lead to erroneous Rayleigh slope extraction from observations, which could potentially influence estimates of, e.g., bulk atmospheric composition or/and atmospheric dust and aerosols/hazes.
2. No significant  $\text{H}_2\text{O}$  absorption feature can be seen in our modeled transmission spectra. This is because  $\text{H}_2\text{O}$  absorption bands are strongly overlapped by  $\text{CH}_4$  and  $\text{CO}_2$  absorption, which occurs higher up in the atmosphere, thus making these spectral regions opaque for radiation. One would need high-resolution spectroscopy to infer  $\text{H}_2\text{O}$  from near-mid IR transmission spectroscopy of such planets.
3. Results suggest  $\text{HNO}_3$  spectral features become apparent in the mid- and far-IR, similar to results discussed in Tabataba-Vakili et al. (2016) and Scheucher et al. (2018). These features might not only be an indicator for SPEs bombarding a planet with an  $\text{N}_2\text{-O}_2$  atmosphere, but could potentially be used as an indirect hint for the presence of  $\text{H}_2\text{O}$  where one cannot see its absorption features in the spectrum.
4.  $\text{O}_3$  features are rather weak for scenarios around quiescent mid-late type M-dwarfs. This arises mainly due to photochemical responses due to the different stellar spectrum (see, e.g., Segura et al. 2005; Grenfell et al. 2012). The weakened ozone features are then even further reduced by SEPs.
5. We calculate a  $5.3 \mu\text{m}$  feature with similar strength in both our nonflaring as well as flaring star runs. This comes from a weak  $5.35 \mu\text{m}$  absorption band of  $\text{CO}_2$  and overlaps strongly with the  $5.3 \mu\text{m}$  NO absorption feature that is evident after SEP events on Earth. Therefore one might misinterpret the presence of such a feature as an Earth-like  $\text{N}_2\text{-O}_2$  atmosphere under strong SEP bombardment.

In a nutshell, we applied our extensive model suite to study the influence of cosmic rays on Prox Cen b as a potentially Earth-like planet and identified some interesting spectral features with strong potential for general characterization and misinterpretation of atmospheric compositions of Earth-like planets in the HZ around M stars.

M.Sch. acknowledges support from DFG project RA 714/9-1. K.H. and J.L.G. acknowledge the International Space Science Institute and the supported International Team 464: *The Role Of Solar And Stellar Energetic Particles On (Exo) Planetary Habitability (ETERNAL, <http://www.issibern.ch/teams/exoeternal/>)*. V.S. and M.Si. acknowledge support from DFG project SI 1088/4-1. F.S. acknowledges support from DFG project SCHR 1125/3-1.

*Software:* GARLIC (Schreier et al. 2014, 2018a, 2018b), HITRAN2016 (Gordon et al. 2017), MPI Mainz Spectral Atlas (Keller-Rudek et al. 2013).

### ORCID iDs

M. Scheucher  <https://orcid.org/0000-0003-4331-2277>

K. Herbst  <https://orcid.org/0000-0001-5622-4829>

J. L. Grenfell  <https://orcid.org/0000-0003-3646-5339>

F. Schreier  <https://orcid.org/0000-0001-7196-6599>

B. Heber  <https://orcid.org/0000-0003-0960-5658>

M. Sinnhuber  <https://orcid.org/0000-0002-3527-9051>

### References

- Airapetian, V. S., Glocer, A., Khazanov, G. V., et al. 2017a, *ApJL*, **836**, L3
- Airapetian, V. S., Jackman, C. H., Mlynczak, M., Danchi, W., & Hunt, L. 2017b, *NatSR*, **7**, 14141
- Anglada-Escudé, G., Amado, P. J., Barnes, J., et al. 2016, *Natur*, **536**, 437
- Banjac, S., Herbst, K., & Heber, B. 2019, *JGRA*, **124**, 50
- Berdyugina, S. V., & Kuhn, J. R. 2019, *AJ*, **158**, 246
- Bétrémieux, Y., & Kaltenegger, L. 2013, *ApJL*, **772**, L31
- Clough, S., Kneizys, F., & Davies, R. 1989, *AtmRe*, **23**, 229
- Cohen, O., Drake, J. J., Glocer, A., et al. 2014, *ApJ*, **790**, 57
- Desorgher, L., Flückiger, E. O., & Gurtner, M. 2006, in 36th COSPAR Scientific Assembly, **2361**
- Dong, C., Lingam, M., Ma, Y., & Cohen, O. 2017, *ApJL*, **837**, L26
- Dorman, L. I., Pustil’Nik, L. A., Sternlieb, A., et al. 2004, *ITPS*, **32**, 1478
- Gordon, I., Rothman, L., Hill, C., et al. 2017, *JQSRT*, **203**, 3
- Grenfell, J. L., Grießmeier, J.-M., von Paris, P., et al. 2012, *AsBio*, **12**, 1109
- Herbst, K., Grenfell, J., Sinnhuber, M., et al. 2019a, *A&A*, **631**, A101
- Herbst, K., Kopp, A., & Heber, B. 2013, *AnGeo*, **31**, 1637
- Herbst, K., Papaioannou, A., Banjac, S., & Heber, B. 2019b, *A&A*, **621**, A67
- Howard, W. S., Tilley, M. A., Corbett, H., et al. 2018, *ApJL*, **860**, L30
- Keller-Rudek, H., Moortgat, G. K., Sander, R., & Sørensen, R. 2013, *ESSD*, **5**, 365
- Lammer, H., Selsis, F., Chassefière, E., et al. 2010, *AsBio*, **10**, 45, pMID: <https://www.ncbi.nlm.nih.gov/pubmed/20307182>
- Manabe, S., & Wetherald, R. T. 1967, *JATs*, **24**, 241
- Marq, E., Belyaev, D., Montmessin, F., et al. 2011, *Icar*, **211**, 58
- Massie, S., & Hunten, D. 1981, *JGRC*, **86**, 9859
- Meadows, V. S., Arney, G. N., Schwieterman, E. W., et al. 2018, *AsBio*, **18**, 133, pMID: <https://www.ncbi.nlm.nih.gov/pubmed/29431479>
- Murphy, W. F. 1977, *JChPh*, **67**, 5877
- Nieder, H., Winkler, H., Marsh, D. R., & Sinnhuber, M. 2014, *JGRA*, **119**, 2137
- Porter, H. S., Jackman, C. H., & Green, A. E. S. 1976, *JChPh*, **65**, 154
- Rauer, H., Gebauer, S., Paris, P. V., et al. 2011, *A&A*, **529**, A8
- Reid, I. N., & Hawley, S. L. 2005, *New Light on Dark Stars: Red Dwarfs, Low-Mass Stars, Brown Dwarfs* (Berlin: Springer)
- Rodler, F., & López-Morales, M. 2014, *ApJ*, **781**, 54
- Sadovskii, A. M., Struminsky, A. B., & Belov, A. 2018, *AstL*, **44**, 324
- Scalo, J., Kaltenegger, L., Segura, A., et al. 2007, *AsBio*, **7**, 85, pMID: <https://www.ncbi.nlm.nih.gov/pubmed/17407405>
- Scheucher, M., Grenfell, J., Wunderlich, F., et al. 2018, *ApJ*, **863**, 6
- Schreier, F., Gimeno García, S., Hedelt, P., et al. 2014, *JQRST*, **137**, 29
- Schreier, F., Milz, M., Buehler, S. A., & von Clarmann, T. 2018a, *JQSRT*, **211**, 64
- Schreier, F., Städt, S., Hedelt, P., & Godolt, M. 2018b, *MolAs*, **11**, 1
- Segura, A., Kasting, J. F., Meadows, V., et al. 2005, *AsBio*, **5**, 706
- Segura, A., Walkowicz, L. M., Meadows, V., Kasting, J., & Hawley, S. 2010, *AsBio*, **10**, 751
- Simon Wedlund, C., Gronoff, G., Lilensten, J., Ménager, H., & Barthélemy, M. 2011, *AnGeo*, **29**, 187
- Sinnhuber, M., Nieder, H., & Wieters, N. 2012, *SGeo*, **33**, 1281
- Sneep, M., & Ubachs, W. 2005, *JQSRT*, **92**, 293
- Snellen, I. 2014, *RSPTA*, **372**, 20130075
- Struminsky, A., Sadovskii, A., & Belov, A. 2017, *Cosmic Rays near Proxima Centauri b, v2*, *Zenodo*,
- Tabataba-Vakili, F., Grenfell, J. L., Grießmeier, J.-M., & Rauer, H. 2016, *A&A*, **585**, A96
- Thébaud, E., Finlay, C. C., Beggan, C. D., et al. 2015, *EP&S*, **67**, 79
- Tilley, M. A., Segura, A., Meadows, V. S., Hawley, S., & Davenport, J. 2019, *AsBio*, **19**, 64
- Turbet, M., Leconte, J., Selsis, F., et al. 2016, *A&A*, **596**, A112
- Valencia, D., Sasselov, D. D., & O’Connell, R. J. 2007, *ApJ*, **665**, 1413
- Vidotto, A. A., Jardine, M., Morin, J., et al. 2013, *A&A*, **557**, A67
- von Paris, P., Selsis, F., Godolt, M., et al. 2015, *Icar*, **257**, 406
- Winkler, H., Kazeminejad, S., Sinnhuber, M., Kallenrode, M. B., & Notholt, J. 2009, *JGRD*, **114**, D00I03